Optical line shapes of color centers in solids from classical autocorrelation functions

Check for updates

Christopher Linderälv[1,2], Nicklas Österbacka [1], Julia Wiktor [1] & Paul Erhart [1] ✉

Color centers play key roles in, e.g., solid state lighting and quantum information technology. Here, we describe an approach for predicting the optical line shapes of such emitters based on direct sampling of the underlying autocorrelation functions through molecular dynamics simulations (MD-ACF). The energy landscapes are represented by a machine-learned potential that describes both the ground and excited state landscapes through a single model, guaranteeing size-consistent predictions. We apply this methodology to the $(V_{Si}V_C)^0_{kk}$ divacancy defect in 4H-SiC and demonstrate that at low temperatures, the present MD-ACF approach reproduces results from the traditional generating function approach. Unlike the latter, it is, however, also applicable at high temperatures as it avoids harmonic and parallel-mode approximations and can be applied to study non-crystalline materials. The MD-ACF methodology thus promises to substantially widen the range of computational predictions of the optical properties of color centers and related defects.

Color centers in solids are not only the source of the luminous appearance of many gemstones but have also found numerous and widespread technological applications as a platform for harnessing the quantum nature of light. This includes, for example, certain types of lasers[1,2], phosphors for solid-state lighting[3,4], and scintillators for radiation detection[5,6]. Furthermore, color centers are emerging as one of the most promising platforms for realizing quantum technologies[7–9], enabling optical initialization and read-out[10] as well as single photon emission[11–13]. Finally, the sensitivity of the optical properties of color centers to changes in external parameters such as temperature, strain, and electromagnetic fields enables applications in sensing[14]. Consequently, the optical line shapes of color centers have become a crucial characteristic, prompting both extensive experimental[15–18] and theoretical efforts[19–22].

The by far most common methodology for predicting line shapes is based on the generating function (GF) approach[23,24] in combination with density functional theory (DFT) calculations. This method has been shown to yield optical line shapes in good agreement with experiments at low temperatures for various color centers[19,20,22,25–30]. Additional developments to account (partially) for temperature[22], the Jahn-Teller effect[28], and the restriction to a one-dimensional configuration coordinate[31] have further increased the value of this method, and currently, it can be considered the reference approach for assessing optical line shapes of color centers in solids. The GF approach, however, involves a number of critical approximations, which can be understood as restrictions on the shapes of and the relation between the ground and excited state potential energy surfaces (PESs) as

well as the treatment of anharmonicity. As discussed below, these approximations limit the reliability of GF predictions at higher temperatures, for anharmonic and/or ionic materials, and in the case of symmetry-breaking electronic excitations.

Here, we describe a methodology that overcomes several of the most crucial limitations of the GF approach, allows one to properly handle the aforementioned cases, and is also applicable to non-crystalline materials. To this end, we combine autocorrelation function (ACF) analysis based on molecular dynamics (MD) simulations with a machine-learning potential (MLP) that can handle both the ground and excited state landscapes (Fig. 1). We demonstrate the utility of this MD-ACF scheme by its application to the $(V_{Si}V_C)^0_{kk}$ divacancy in 4H-SiC (Fig. 2). This prototypical color center has been extensively studied both experimentally[22,32,33] and computationally[21,22], thanks to its potential for applications in quantum technology[33–36]. This defect serves as an ideal benchmark for the present approach, enabling a careful comparison with the GF method while providing a challenging test case.

The remainder of this paper is organized as follows. First, we review the GF framework and the ACF approach before introducing a scheme for the construction of an MLP that can handle both ground and excited states. These elements are then combined to analyze the optical fine structure of the aforementioned divacancy defect in 4H-SiC. We provide a detailed discussion of the approximations that are employed and their impact on the predicted line shapes before closing with an outlook into possible future developments.

[1]Department of Physics, Chalmers University of Technology, Gothenburg, Sweden. [2]Department of Physics/Centre for Materials Science and Nanotechnology, University of Oslo, Oslo, Norway. ✉e-mail: erhart@chalmers.se
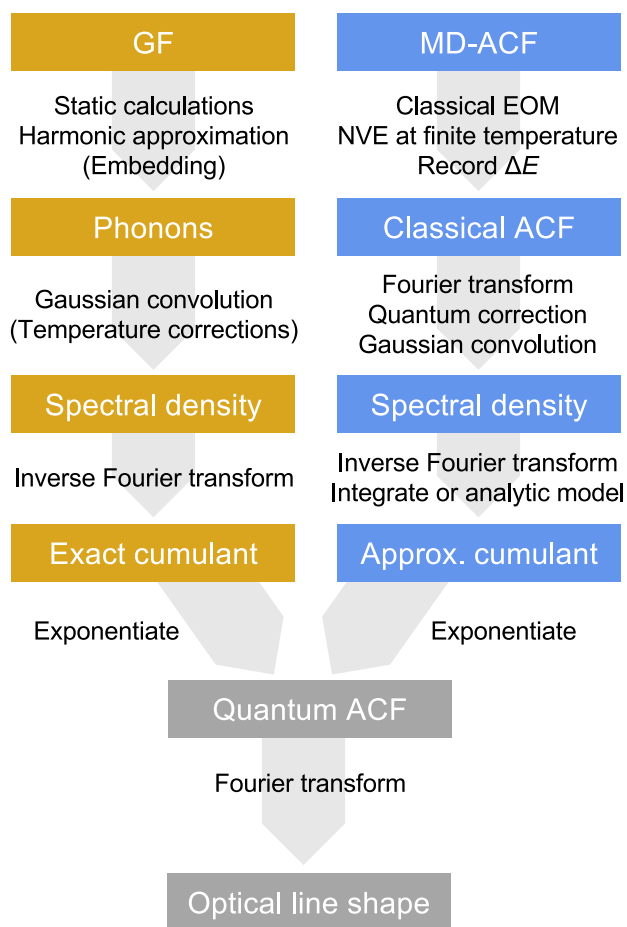
Fig. 1 | Workflows. Illustration of the various steps involved in obtaining the optical line shape from the generating function (GF) method and the method based on molecular dynamics and autocorrelation function analysis (MD-ACF).

Results

Line shape theory

First, we recap the GF approach before describing the ACF methodology. The workflows of the two methods are schematically summarized in Fig. 1.

The starting point for either approach for modeling optical line shapes is Fermi's golden rule, from which the following expression for the optical line shape during emission can be derived[37]

$$I(\omega) \propto \omega^3 A(\omega), \tag{1}$$

where

$$A(\omega) = \int_{-\infty}^{\infty} dt \langle \boldsymbol{\mu}(0)\boldsymbol{\mu}(t)\rangle \exp(i\omega t) \tag{2}$$

is the line shape function and

$$\langle \boldsymbol{\mu}(0)\boldsymbol{\mu}(t)\rangle = C(t) \tag{3}$$

is the dipole-dipole ACF.

The GF approach

The GF approach is based on the (i) parallel-mode, (ii) Franck-Condon, and (iii) harmonic approximations, where we note that the Franck-Condon approximation includes the constant dipole approximation as discussed at the end of this section. Most of these approximations can be understood as restrictions on the PESs (Fig. 2d–e). The harmonic approximation means that both PESs are perfectly quadratic. The parallel-mode approximation further assumes that there is a one-to-one correspondence between modes in the ground and excited state and that the PESs are simply displaced with respect to each other. Furthermore, the curvature of the PESs is assumed to be exactly the same. This has to be true for each of the $3N$ vibrational modes. These are, in general, rather strict requirements that can cause a qualitative disparity between calculations and experiments.

In the GF approach, the dipole-dipole ACF then takes the form[19]

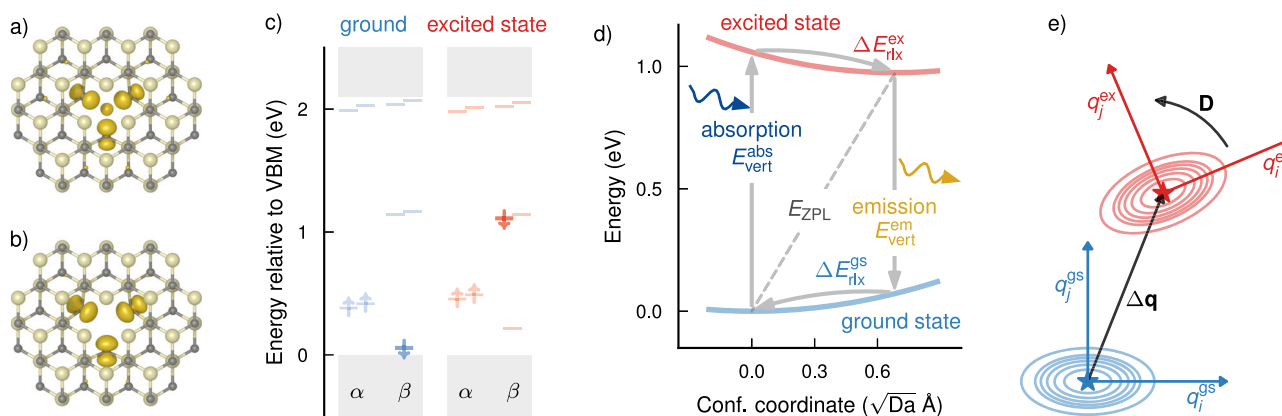$$C(t) = \exp(S(t) - S(0)), \tag{4}$$

Fig. 2 | Ground and excited landscapes of the $(V_{Si}V_C)^0_{kk}$ defect. Defect configuration in **a** ground and **b** excited state. The charge density of the localized electronic states that are occupied in the respective configurations and highlighted in (**c**) are shown by isosurfaces (also see Figs. S1 and S2 (See Supplemental Material at [https://doi.org/10.1038/s41524-025-01565-x] for computational and technical details, a short discussion of the prefactor used in the calculation of the spectral density $\hat{j}_{cl}(\omega)$ as well as additional figures.)). **c** Level structure according to the Kohn-Sham eigenstates. The localized levels shown in (**a**, **b**) are highlighted by bold bars in the β spin channel. **d** Illustration of the simplified treatment of the configuration coordinate in the parallel-mode approximation commonly used in the GF approach, which reduces the $3N$-dimensional configuration coordinate to one dimension. The minima on the ground and excited state landscapes correspond to the atomic configurations shown in (**a**) and (**b**), respectively, and their distance equals Δq. The figure also indicates the vertical excitation energies E_{vert}, the ZPL energy E_{ZPL} as well as the Stokes shifts ΔE_{rlx}. **e** Illustration of the more general relationship between the ground and excited state normal modes. In this case, the normal modes corresponding to the ground (gs) and excited state (ex) are translated by a vector Δq and rotated by the Duschinsky matrix **D**.

where $S(t)$ is the inverse Fourier transform of the electron-phonon spectral function

$$S(\omega) = \sum_k s_k \, \delta(\omega - \omega_k). \tag{5}$$

Here, s_k is the partial Huang-Rhys factor defined as

$$s_k = \frac{1}{2} \, \omega_k \, \Delta q_k^2, \tag{6}$$

where Δq_k is the projection of the ionic configurational difference $\Delta \boldsymbol{R}$ on phonon mode k given by

$$\Delta q_k = \sum_a \sqrt{m_a} \, \langle \boldsymbol{n}_k^a | \Delta \boldsymbol{R}_a \rangle. \tag{7}$$

Here, a runs over all the atoms in the system, m_a is the mass, and $|\boldsymbol{n}_k\rangle$ is the normalized ionic displacement vector corresponding to phonon mode k.

The expression for the ACF in Eq. (4) is obtained under the assumptions that the ground and excited state phonon modes are parallel as well as harmonic, that emission occurs from the vibrational ground state (i.e., low temperature), and that the Franck-Condon approximation holds. While the low-temperature assumption can to some extent be relaxed by including Bose-Einstein statistics in the correlation function[22], the other approximations remain difficult to avoid and even control a priori. For example, the evaluation of the partial Huang-Rhys factors according to Eq. (6) strictly requires the phonon modes k in the ground and excited states to have the same frequency and to be linearly related.

In general, the eigenvectors of the phonon modes of the ground state $\boldsymbol{q}^{\mathrm{gs}}$ and the excited state $\boldsymbol{q}^{\mathrm{ex}}$ are related by a rotation and displacement

$$\boldsymbol{q}^{\mathrm{ex}} = \mathbf{D}\boldsymbol{q}^{\mathrm{gs}} + \Delta \boldsymbol{q}, \tag{8}$$

where $\mathbf{D}$ is the Duschinsky matrix, which introduces a rotation (or mixing) between the phonon modes in the different electronic states and $\Delta \boldsymbol{q}$ is the displacement between the minima of the ground and excited state PESs (Fig. 2e). In the GF approach, the phonon modes are required to be linearly related, i.e., $q_k^{\mathrm{ex}} = q_k^{\mathrm{gs}} + \Delta q_k$ for some constant Δq_k. This approximation can be particularly severe for symmetry-breaking excitations/deexcitations and/or in systems with pronounced anharmonicity.

Next, the Franck-Condon approximation is based on the zeroth-order term in a series expansion of the dipole moment, and it has been outlined how to include linear terms (Herzberg-Teller factors)[37]. Including the linear terms and using different vibrational modes in the initial and final states adds considerable complexity to the task of evaluating the optical line shapes, and has to the best of our knowledge not been implemented and tested for solid state systems.

The MD-ACF approach

In the physical chemistry community, modeling line shapes from ACFs sampled via classical MD simulations is an established approach, and commonly applied to molecular systems. While this applies predominantly to vibrational spectra related to infrared and Raman measurements[38,39], optical spectra can be obtained as well via mixed quantum-classical approaches[40–42]. At the same time, the possibilities to model materials at the relevant length and time scales have significantly improved in recent years due to the advent of MLPs that are not only accurate and efficient but able to describe systems with increasing chemical, structural, and dynamical complexity.

The starting point is again Eq. (1) and in the Franck-Condon approximation the (quantum) ACF can be cast in the form of a time-ordered exponential[40]

$$C(t) = \left\langle \exp\left(\mathrm{i} \int_0^t \mathrm{d}t' \, U(t') \right) \right\rangle_{\mathrm{ens}},$$

where U is the *gap* operator, i.e., the energy difference between the initial and final state, and the angular brackets indicate an ensemble average. This exponential can be expanded in cumulants as

$$C(t) = \exp\left(\sum_{n=1}^{\infty} g_n(t) \right).$$

For a fully harmonic system, this expansion is truncated at the second order, i.e., g_2 describes the vibrational coupling in a harmonic system exactly[43]. The second-order cumulant contains the information present in the two-time classical ACF of the potential energy difference. It is given by

$$g_2(t) = -\int_0^t \mathrm{d}t' \int_0^{t'} \mathrm{d}t'' \langle \Delta U(0) \, \Delta U(t'') \rangle. \tag{9}$$

The cumulant is then related to the optical line shape function as

$$A(\omega) = \int_{-\infty}^{\infty} \mathrm{d}t \, \exp[\mathrm{i}(\omega - \underbrace{(E_{\mathrm{vert}} \mp \Delta E_{\mathrm{rlx}})}_{E_{\mathrm{ZPL}}})t] \, \exp[-g_2(t)], \tag{10}$$

which is centered at the ZPL energy, E_{ZPL}, i.e., the energy obtained from the vertical transition energy $E_{\mathrm{vert}} > 0$ and the relaxation energy (or one-sided Stokes shift) $\Delta E_{\mathrm{rlx}} > 0$ where $-/+$ are applicable for absorption and emission, respectively (Fig. 2d).

In order to obtain the cumulant, we start from the energy difference of the adiabatic PESs corresponding to the initial and final electronic states. The energy difference function can be computed from a classical trajectory propagated with the Hamiltonian corresponding to the initial state. By propagating on the ground or excited state PES we can thus model absorption or emission spectra, respectively.

The classical energy gap operator is

$$\Delta U_{\mathrm{cl}}(t) = U_{\mathrm{cl}}^{\mathrm{ex}}(\boldsymbol{R}(t)) - U_{\mathrm{cl}}^{\mathrm{gs}}(\boldsymbol{R}(t)) \\ - \langle U_{\mathrm{cl}}^{\mathrm{ex}}(\boldsymbol{R}(t)) - U_{\mathrm{cl}}^{\mathrm{gs}}(\boldsymbol{R}(t)) \rangle,$$

where $\boldsymbol{R}(t)$ is the atomic configuration of the system at time t, $\langle \cdot \rangle$ is the average vertical transition energy $\langle E_{\mathrm{vert}} \rangle$, and U is the potential energy of the system. The energy ΔU_{cl} thus corresponds to the difference in vibrational energy between the initial and final states.

The classical ACF of ΔU_{cl} is the projection of $\Delta U_{\mathrm{cl}}(t)$ on $\Delta U_{\mathrm{cl}}(0)$, i.e.,

$$C_{\mathrm{cl}}(t) = \langle \langle \Delta U_{\mathrm{cl}}(t) \Delta U_{\mathrm{cl}}(0) \rangle_{\tau} \rangle_{\mathrm{ens}}, \tag{11}$$

where the inner and outer angular brackets indicate an average over time origins and an ensemble average, respectively.

Since $C_{\mathrm{cl}}(t)$ is symmetric in time, the imaginary part of the classical ACF is zero, in contrast to the quantum ACF. This is related to the phonons in the quantum case carrying a phase as well as the time-energy uncertainty. The imaginary part of the quantum ACF can, however, be reconstructed to some extent a posteriori from the classical ACF (see the prefactor in Eq. (13) below)[42].

Similar to the GF approach we apply a broadening to the ACF to mimic the effect of the instrumental resolution function by convolution with a Gaussian function,

$$\widetilde{C}_{\mathrm{cl}}(t) = C_{\mathrm{cl}}(t) \exp(-\gamma t^2). \tag{12}$$

Accordingly we work out the second-order cumulant from $\widetilde{C}_{\mathrm{cl}}$ instead of the bare C_{cl}, which smoothens the Fourier transform of the latter, i.e., the

spectral density Eq. (13). This has a similar effect on the spectral density as the approximation of the δ-functions in Eq. (5) with normalized Gaussians.

The spectral density function $\hat{j}_{cl}(\omega)$ is given by[42]

$$\hat{j}_{cl}(\omega) = \theta(\omega)\,\frac{1}{\pi}\,f(\beta\omega)\,\widetilde{C}_{cl}(\omega), \tag{13}$$

where $\theta(\omega)$ is the Heaviside function. Note that there are several possibilities for choosing the prefactor $f(\beta\omega)$ to include approximate quantum effects[42,44] (see Methods). In this work, we use the harmonic prefactor $\beta\omega/2$, which yields results that are consistent with GF calculations[22] and has also been found to be a suitable choice in calculations for the Fenna-Matthews-Olson complex[42]. We emphasize that using the harmonic prefactor does *not* imply that we assume the system to behave fully harmonic but rather that the treatment of quantum effects is limited to the harmonic approximation.

The Stokes shift, i.e., the relaxation energy on the final state PES (also see Fig. 2d) is[45]

$$\Delta E_{rlx} = \int_0^\infty d\omega\,\frac{\hat{j}_{cl}(\omega)}{\omega}. \tag{14}$$

Furthermore in the mode-decomposed case the following relation holds[42]

$$\hat{j}_{cl}(\omega) = \sum_j \omega_j\,\Delta E_{rlx,j}\,\delta(\omega - \omega_j). \tag{15}$$

In a fully harmonic system, the mode-decomposed Stokes shift can be written in terms of the partial Huang-Rhys factors as $\Delta E_{rlx,j} = \omega_j s_j$. This yields

$$\hat{j}_{cl}(\omega) = \frac{1}{2}\sum_j \omega_j^2\,s_j\,\delta(\omega - \omega_j), $$

which shows that

$$F(\omega) = \hat{j}_{cl}/\omega^2 \tag{16}$$

plays a similar role as the electron-phonon spectral function $S(\omega)$ in the GF approach, see Eq. (5), provides a natural relation between the electron-phonon spectral function in Eq. (5) and the spectral density computed at finite temperatures. The relation between the spectral density $F(\omega)$ (or equivalently $\hat{j}_{cl}(\omega)$) and the second-order cumulant $g_2(t)$, see Eq. (9), is[46]

$$g_2(t) = -\int_{-\infty}^{\infty} d\omega\,F(\omega)\Big\{\coth\Big(\frac{\beta\omega}{2}\Big) \\ [\cos(\omega t) - 1] - i[\sin(\omega t) - \omega t]\Big\}. \tag{17}$$

The MD-ACF approach as expressed through Eqs. (11) to (17) relies on the following approximations: (*i*) the truncation of the cumulant expansion at second order, (*ii*) the reconstruction of the quantum time ACF from the classical ACF, and (*iii*) the Franck-Condon approximation as discussed in ref. 46.

A MLP for ground and excited states

In 4H-SiC Si and C occupy two symmetry inequivalent sites, commonly referred to as *h* and *k*. There are thus four different divacancy configurations, corresponding to the combinations (*h*, *h*), (*h*, *k*), (*k*, *h*), and (*k*, *k*). In this study, we consider the $(V_{Si}V_C)^0_{kk}$ divacancy in 4H-SiC (Fig. 2), which hosts a bright transition and has been studied both experimentally and computationally[33,47,48]. This defect features four localized levels in the α-spin channel and five localized levels in the β-spin channel that are occupied by two and one electron(s), respectively (Fig. 2c; also see Figs. S1 and S2). In the ground state, the lone electron in the β-channel occupies the lowermost level, while in the first excited state, it is promoted to the next higher orbital, which is very nearly degenerated with the next-next higher orbital.

Using DFT calculations and a 286-atom supercell we obtain a vertical excitation energy for absorption of $E_{vert}^{abs} = 1.06$ eV (Fig. 2d) and a ZPL energy of $E_{ZPL} = 0.97$ eV (see Methods for computational details). This is in line with previous theoretical results predicting the ZPL at 1.0 to 1.1 eV using a comparable level of theory and computational settings[22,49].

The MD-ACF approach outlined above relies on a very thorough sampling of both ground and excited PESs to ensure convergence of the results. To this end, one requires sampling over many nanoseconds (see Methods) and systems on the order of a hundred thousand or more atoms. As this is far beyond the domain of ab initio MD simulations, we require an effective yet accurate representation of the PESs, which is, in principle, available via MLPs.

While there are a few examples of excited state models for molecular systems[50,51], in condensed matter MLPs have been so far primarily employed for the description of ground state PESs[52–54]. Since we are dealing with an extended system represented by periodic boundary conditions, additional considerations are required. In particular one must ensure that the formation and excitation energies converge to constant values in the limit of an infinite system. This prohibits the naive approach of constructing separate MLPs for ground and excited PESs. To address this issue, we exploit that the electronic impact of the defect considered here (as well as numerous other defects) is largely limited to its immediate vicinity, as the electronic states of the defect are practically completely localized at the nearest-neighbor atoms of the vacancy (Fig. 2a, b). This allows us to construct a *single* model that can handle *both* the ground and the excited state by treating the nearest-neighbor atoms of the divacancy as separate species. Specifically, we set up an MLP that distinguishes bulk Si and C representing atoms not directly involved with the defect as well as Si_{gs}, C_{gs}, Si_{ex}, and C_{ex}, which represent the nearest neighbors of the divacancy in the ground (gs) and excited state (ex), respectively.

We adopt the NEP framework[55–57] to construct the MLP as NEP models have proven to be not only accurate but also computationally very efficient, which is an important consideration for the present application. The reference data includes both pristine (defect-free) and defective structures with varying sizes, energies, and forces from DFT calculations. The final MLP accurately reproduces the reference DFT data for ideal (defect-free) structures as well as defect structures in both the ground and excited state as evident from parity plots as well as the root mean square errors (RMSEs) and coefficients of determination R^2 (Figs. 3a and S3). The model also predicts a phonon dispersion in good with DFT calculations (Fig. 3b) and the PESs along the configuration coordinate closely match the reference data for both ground and excited states (Fig. 3c). For the 286-atom cell used for this comparison, we obtain vertical excitation energies of 1.01 eV and 1.06 eV from NEP and DFT calculations, respectively, as well as ZPL energies of 0.94 eV and 0.97 eV, with $\Delta q = 0.68\,\sqrt{Da}$Å in both cases. This implies that also the Stokes shifts on the ground and excited state landscape are in good agreement (Fig. 3c).

The vertical excitation energy for absorption E_{vert}^{abs}, ZPL energy E_{ZPL}, and formation energy E_f from the NEP calculations vary smoothly with system size and converge to constant values as the number of atoms goes to infinity, $N \to \infty$ (Fig. 4a). For system sizes above ~2000 atoms the energies deviate by less than 1 meV from their converged values. The Stokes shifts converge to 71 meV and 80 meV for the ground and excited states, respectively. We also note that the converged ZPL energy of 0.91 eV is in good agreement with DFT calculations using the PBE exchange-correlation functionals for a 2400-atom supercell, which yielded a value of 0.94 eV[49].

Compared to the energetics, the displacement Δq exhibits a more pronounced system size dependence, as it increases from $0.68\,\sqrt{Da}$Å for a 286-atom cell to $0.81\,\sqrt{Da}$Å in the limit $N \to \infty$. This increase can be understood by recalling that even small displacements far from the defect contribute to Δq and is a testament to the long-ranged (albeit small) elastic strains induced by the defect.

Sampling the spectral density

Having demonstrated the ability of the MLP to describe both the ground and excited state PESs on a common footing, we can deploy it in the context
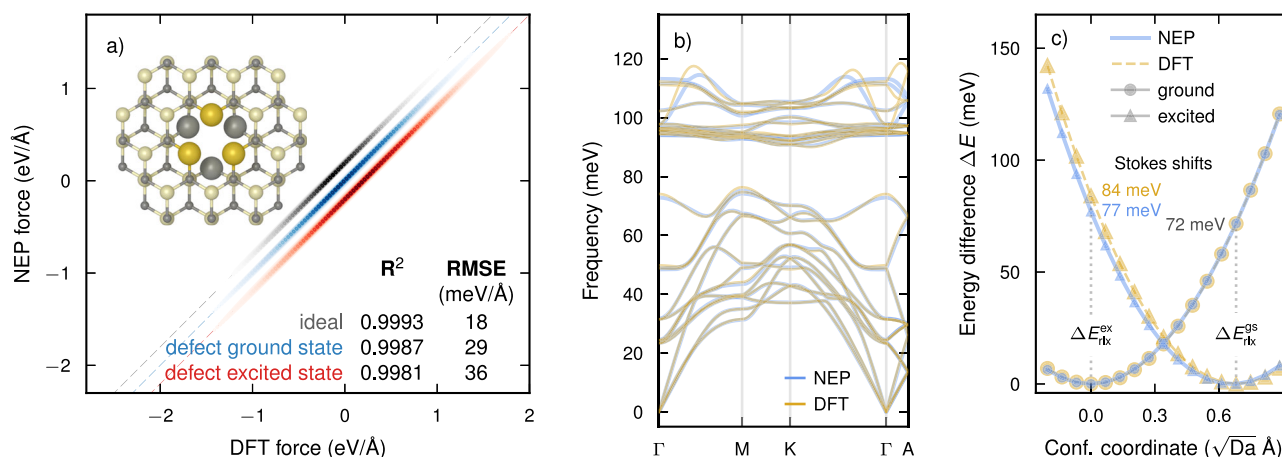
Fig. 3 | Machine-learning potential model for ground and excited state defect energetics. a Parity plots in the form of kernel density estimates for the force components comparing results from the machine-learning potential based on the neuroevolution potential (NEP) framework constructed in this work with DFT reference data (also see Fig. S3). Coefficients of determination (R^2) and root mean square errors (RMSEs) for subsets of the data are shown in the table. The inset illustrates the defect decoration approach with Si and C atoms associated with the defect shown as large yellow and dark gray atoms. **b** Phonon dispersion for the pristine primitive cell from the NEP model and DFT calculations ($6 \times 6 \times 2$ supercell, 576 atoms). **c** 1D configurational coordinate diagram computed for the ground and excited state of the divacancy (286-atom supercells relaxed with DFT). For ease of comparison, the energy difference ΔE is shown with respect to the minimum of each curve. The Stokes shifts ΔE_{rlx} on the excited (ex) and ground state (gs) landscape from NEP and DFT calculations are indicated.
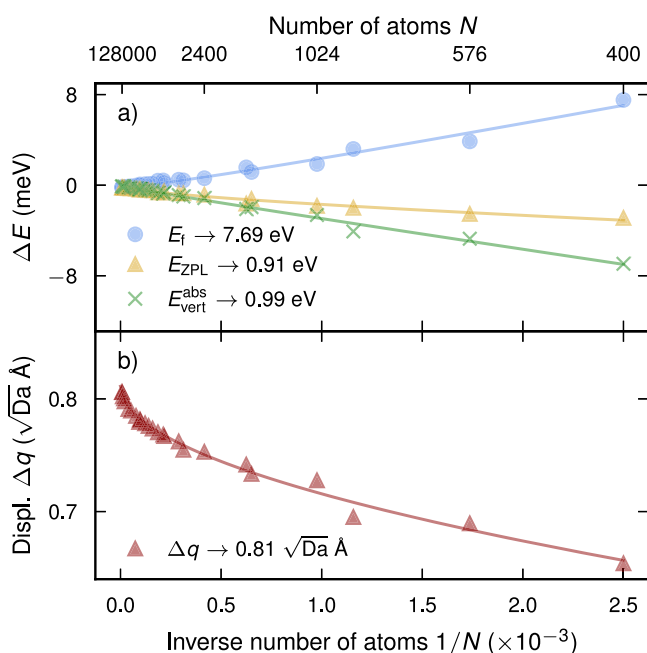
Fig. 4 | Size convergence of various defect-related properties. a Variation of the formation energy E_f, ZPL energy E_{ZPL}, vertical excitation energy for absorption $E_{\text{vert}}^{\text{abs}}$, and **b** the displacement Δq with the number of atoms N in the supercell; see Fig. 2d for the definition of these quantities. Since the leading interaction between defects is due to strain, which scales with the distance L between defects approximately as $1/L^3 \sim 1/V^3$, the scaling is shown as a function of the inverse number of atom $1/N$.

Fig. 5 | Spectral density. Spectral densities obtained by propagation on the ground and excited state PESs at different temperatures using Gaussian broadening with a width of $\gamma = 1.5$ meV, see Eq. (12). The vertical dashed gray lines indicate the center of the main bands in the spectral density for the excited state. See Fig. S4a, b for an illustration of the effect of broadening.

of the MD-ACF framework. To this end, we first carried out MD simulations on both the ground and excited state PESs at temperatures of 70, 150, and 300 K using supercells with more than 1,000,000 atoms (see Methods for further details). These computational parameters were obtained through careful testing. We note that large system sizes are needed to ensure a dense sampling of the phonon dispersion relative to the Brillouin zone, and also help in reducing the noise in the ACF. Thanks to the thin architecture of the NEP methodology and its efficient implementation on GPUs, the computer time requirements are still modest.
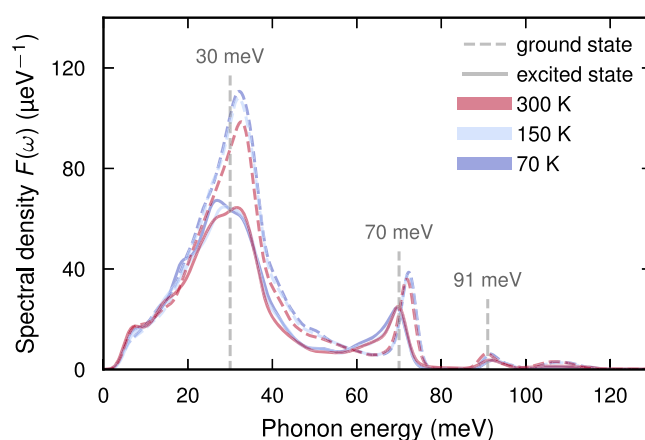
Using Eq. (11) we computed the classical ACF from these trajectories, from which the spectral density $F(\omega)$ was obtained via Eqs. (13) and (16). The overall features of the spectral density $F(\omega)$ are consistent for the different temperatures exhibiting a main peak at about 30 meV and a smaller peak at 70 meV (Fig. 5; also see Fig. S4a, b). There are also very minor contributions at higher energies at about 91 meV. It is also apparent that the broadening of the spectra with increasing temperature is readily captured without having to resort to empirical parameters.

The features and the overall shape of the spectral density are consistent with the electron-phonon spectral function $S(\omega)$ in the GF approach given by Eq. (5)[21,22]. We note that a direct comparison of $S(\omega)$ and $F(\omega)$ would be misleading as the latter is computed at finite temperatures, and thus, the treatment of phonon occupation factors is relevant (classical vs quantum statistics).

There are a few differences between the ground state and excited state spectral density functions. When propagating on the excited state PES the integral over the spectral density $F(\omega)$ at 70 K, as a proxy for the total Huang-Rhys factor, is significantly smaller at 1.93, compared with 2.57 for the
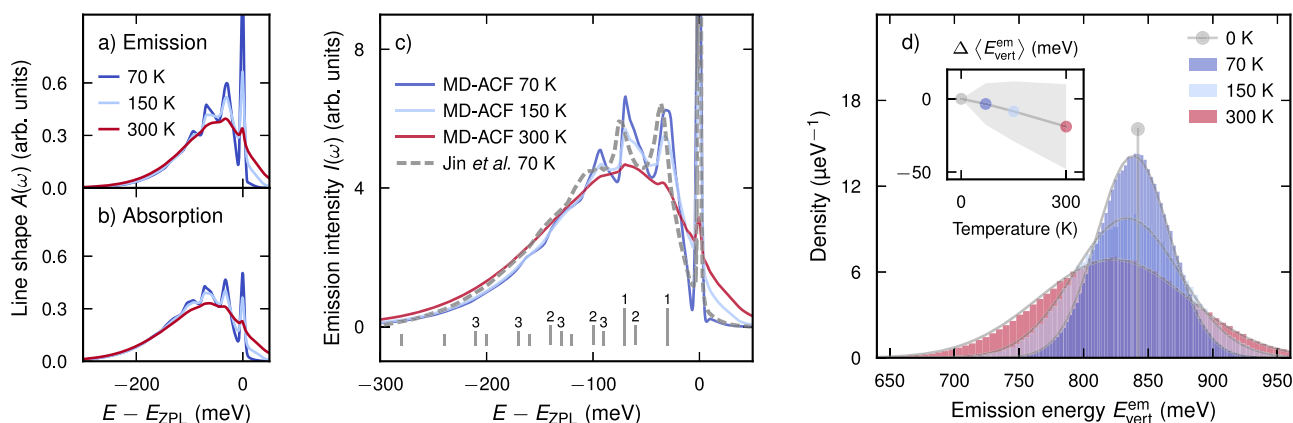
Fig. 6 | Line shape functions and emission spectra. a, b Line shape functions $A(\omega)$ from Eq. (10) obtained by propagation on (**a**) the excited and (**b**) ground state PES to describe emission and absorption, respectively. **c** Emission spectra from the MD-ACF approach described in this work in comparison with calculations using the GF approach by Jin et al.[22]. The vertical gray lines indicate the frequencies that are obtained by combining the bands at 30 meV and 70 meV observable in the spectral density (Fig. 5). The order of the combination is given by the numbers and indicated by the length of the lines. **d** Distribution of vertical transition energies for propagation on the excited state PES. The distributions are rather well described by Gaussians (solid gray lines), indicating that truncating the cumulant expansion at second order is a good approximation in this case. The inset shows the shift of the average emission energy $\langle E_{\text{vert}}^{\text{em}} \rangle$ with respect to the emission energy at 0 K.

ground state case (Fig. 5). These numbers decrease with temperature, with values of 1.89/2.47 at 150 K and 1.85/2.33 at 300 K for the excited/ground state. Furthermore, the main peak and the peak at about 70 meV are slightly red-shifted in comparison with propagation on the ground state PES.

Finally we note that the feature at 70 meV (i.e., before application of Gaussian broadening) is fundamentally actually very narrow ($\lesssim 1$ meV; Fig. S4a, b) whereas the feature at 30 meV has an intrinsic full width-half maximum of about 14 meV. This suggests that the latter is the result of the coupling of many modes whereas the former originates from only one or at most a few modes. The difference is, however, obscured by the Gaussian smearing, which is applied here to mimic instrumental broadening present in experimental measurements.

Emission line shapes from MD-ACF

The emission line shapes $A(\omega)$, see Eq. (10), exhibit a series of sharp features that broaden with increasing temperature (Fig. 6a). The spacing between these features can be understood as resulting from the combination of the bands observable in the spectral density with lower order combinations giving stronger features (Fig. 5). This becomes even more apparent when considering the emission intensity $I(\omega)$, see Eq. (1) (Fig. 6c). The two most prominent sidebands at $\tilde{\omega}_1 = 30$ meV and $\tilde{\omega}_2 = 70$ meV can thus be identified as first-order excitations of the respective bands, while second-order excitations give rise to the shoulders at 60 meV ($2 \times \tilde{\omega}_1$) and 140 meV ($2 \times \tilde{\omega}_2$) as well as the peak at 100 meV ($\tilde{\omega}_1 + \tilde{\omega}_2$).

The features are most pronounced in the spectrum at 70 K, in accordance with published line shapes at 0 K[21] and especially the 70 K spectrum computed using a temperature-extended GF approach with force constants embedding[22]. Overall, the line shape is rather similar, both the intensity of the peaks and the low energy tail. The small remaining deviations can likely be attributed to differences in the computational parameters, in particular the exchange-correlation functionals, as the present work used PBEsol while the DDE functional[58] was employed in ref. 22. Notably, the MD-ACF results capture the significant broadening of the spectrum at 300 K as well as the reduction in the intensity of the ZPL.

One of the main approximations of the MD-ACF method is the assumption that the cumulant expansion can be truncated at the second order. The reliability of this approximation can be checked by investigating the distribution of the emission energies observed during an MD simulation. While one does notice that the distribution becomes slightly asymmetric at 300 K (Fig. 6d), the distributions are still very well represented by Gaussians and hence the truncation at second order is justified in the present case. Our simulations also allow us to obtain the temperature dependence of the

average emission energy $\langle E_{\text{vert}}^{\text{em}} \rangle$ (i.e., the mean of the distributions in Fig. 6d), which we find to red-shift by 19 meV between 0 and 300 K (Fig. 6d, inset).

Here, we do not report absorption spectra due to the degeneracy of the excited states. The latter causes electronic and vibrational states to mix (which is not included in the current model), which in turn prevents a meaningful comparison with experiment. For reference we do, however, include a comparison of the spectral densities from propagation on the ground and excited states (Fig. 6a, b).

Discussion

Beyond the harmonic and parallel-mode approximations

A crucial parameter for any color center is the (total) Huang-Rhys factor. It can be obtained from the displacement Δq via

$$S = \omega_{\text{eff}} \Delta q^2 / 2, \qquad (18)$$

where ω_{eff} is an effective frequency representing the curvature at the minimum of the PES, or equivalently by integrating over the spectral function $S(\omega)$, see Eq. (5). The Huang-Rhys factor has a profound effect on the optical line shape. Smaller values ($S \lesssim 2$) commonly give rise to structured line shapes with distinct peaks whereas large values give rise to wide Gaussian side bands[24].

For applications in lighting, color centers are used to red-shift the energy of absorbed light[59], which requires moderate to large Huang-Rhys factors. By contrast, for applications in quantum information theory, one typically aims for small to moderate Huang-Rhys factors in order to maintain coherent emission. As the displacement between the ground and excited PESs increases (and thus the Huang-Rhys factor), vertical transitions are increasingly likely to terminate in the anharmonic region of the receiving PES. Simultaneously the parallel-mode approximation and the restriction to a one-dimensional configuration coordinate (Fig. 2d) become increasingly questionable. As the MD-ACF approach, in combination with a model for the ground and excited state landscapes, can sample the configuration space over a very wide region, it is not bound by these approximations and is particularly well suited for such cases. Here, we have chosen a defect with an intermediate Huang-Rhys factor of 2.5 to 2.8 at 0 K[22] as it provides a good reference point to demonstrate and benchmark the MD-ACF approach. We emphasize, however, that the latter should be even more powerful when applied to systems with larger Huang-Rhys factors, stronger anharmonicity, and/or large differences in the vibrational structure of ground and excited state.

In the limit of exactly parallel modes the line shape function $A(\omega)$ is symmetric around $\omega = 0$. For the $(V_{Si}V_C)^0_{kk}$ defect considered here, the differences in the line shape function $A(\omega)$ obtained by propagation on the ground and excited state PESs (Fig. 6) reveal, however, an asymmetry and thus the limitation of the parallel-mode approximation even in this relatively simple case. The asymmetry is also apparent in the Huang-Rhys factor, which can be approximately measured by the integral of $F(\omega)$, which equals 1.93 for emission and 2.57 for absorption at 70 K. While these numbers cannot be compared *directly* with the GF approach (see comment following Eq. (16)), we note that they are comparable to the 0 K Huang-Rhys factor of 2.5–2.8 obtained in ref. 22. The latter reference also analyzed the limitations of the parallel-mode approximation using a one-dimensional model with different effective frequencies for ground and excited states. It was concluded that the difference of ~5 meV resulted in minor errors at lower temperatures but in non-negligible errors at high temperatures. While this points in a similar direction as the present analysis, our results suggest that differences might already be noticeable at lower temperatures.

The spectral densities obtained by propagation on the ground and excited landscapes exhibit some notable differences (Fig. 6a, b), which implies that the optical line shapes are also different. In terms of the efficiency of the sampling we note that it is still unclear which PES should be chosen for propagating the system in general[40]. In this context, the expressions for the cumulant for propagating the system on the final or even an average of the initial and final PES for the emission process have been provided in the literature[40]. The choice of PES to propagate on may ultimately be system-dependent and a matter of sampling. For this system, however, propagation on the initial state PES provides a very good agreement with other theoretical work and measurements of the emission line shape[22].

Modeling ground and excited state landscapes
We have introduced a simple yet effective procedure for constructing MLPs that can accurately handle ground and excited states in a computationally efficient manner. It can be straightforwardly extended to include further excited states by adding corresponding "marker" species. The approach is generally applicable to defects and related excitations, such as self-trapped excitons and polarons, as long as they do not diffuse over the relevant time scales at the temperatures of interest. This category includes a huge number of cases, opening the possibility to quantitatively study the opto-vibrational coupling in these systems at elevated temperatures, a challenge that dates back to the early work by Born and Huang[60].

Outlook
In this work we have described an approach for predicting the optical spectra of defects that overcomes the restrictions on the ground and excited landscapes common in calculations based on the GF approach and is also applicable to non-crystalline materials. In this approach, the ACF of the gap operator is sampled through MD simulations using an MLP based on the NEP framework to model the ground and excited state landscapes. As this approach is not limited by constraints on the relation between the initial and final state landscapes commonly required in the GF methodology, it should be particularly suitable for studying systems at higher temperatures, with pronounced anharmonicity, and/or large differences between the initial and final landscapes. The present work thus represents an important step towards a more comprehensive description of the coupling between radiative transitions and vibrational degrees of freedom in condensed matter systems.

Furthermore, we envision that the MD-ACF approach can be extended to capture additional elusive effects. This includes, e.g., the commonly used assumption of a constant transition dipole moment, as the latter can be represented through a machine-learning model using, for example, the tensorial NEP formalism[39]. This would allow one to sample the dipole-dipole ACF directly, see Eq. (3), as commonly done when predicting infrared spectra of molecules and liquids. Moreover the dissipative dynamics that lead to ZPL broadening may be possible to address by

including higher-order cumulants[43]. This would require additional algorithmic development since already three-time correlation functions are prohibitively expensive to calculate directly for long-time series. In this context, we note that it might also be possible to approximate the quantum ACF and bypass the phenomenological prefactor via path integral MD in the form of, e.g., ring polymer or Matsubara dynamics[61].

Finally, we recall that the current approach for constructing models for ground and excited PESs is limited to (the large class of) immobile (non-diffusing) defects. It does, however, indicate a potential pathway for generalizing the construction of MLP models that are not subject to this constraint.

Methods
DFT calculations
Collinear spin-polarized DFT calculations were performed using the projector augmented wave method[62,63] as implemented in the Vienna ab-initio simulation package[64–66] with a plane wave energy cutoff of 520 eV and the PBEsol exchange-correlation functional[67]. The Brillouin zone was sampled with automatically generated Γ-centered $\boldsymbol{k}$-point grids with a maximum spacing of 0.25 Å^{-1}. The excited state was obtained by enforcing the occupation of the first defect level in the β-spin channel to zero (β, $n = 1$ in Fig. S2) and the occupation of the second level to one (β, $n = 2$ in Fig. S2) as in ref. 22.

Construction of the machine-learned potential
We constructed an MLP model using the NEP framework[55–57] and the iterative strategy outlined in ref. 52 utilizing the GPUMD[57] and CALORINE packages[68]. Training structures included configurations along the configuration coordinate (Fig. 2d) as well as snapshots of ideal and defective structures for a range of system sizes and supercell shapes generated via an active learning strategy. To this end, MD simulations were carried out between 70 and 600 K and at pressures ranging from −2.5 to 10 GPa using the respective most recent generation of the NEP model. We then randomly selected snapshots from these trajectories, for which we computed reference energies, forces, and stresses via DFT. These configurations were subsequently included when training the next-generation NEP model. In total the training set consisted of 1341 structures, corresponding to a total of 448388 atoms, including 59 defect-free configurations as well as 641 configurations each of defect structures on the ground and excited state PESs. Structure generation and manipulation were carried out using the ASE[69] and HI-PHI-VE packages[70].

The final NEP model was obtained after three iterations and trained using all available reference data. In addition, we trained an ensemble model using five folds to estimate the model error via k-fold cross-validation. The resulting RMSEs are 0.170(4) meV atom^{-1} for the energies and 32.1(8) meV Å^{-1} for the forces. The corresponding average coefficients of determination on the same folds are $R^2 = 0.999980(6)$ and $R^2 = 0.99800(3)$ for energies and forces, respectively (Fig. S3).

Phonon dispersions for the ideal structure (Fig. 3b) were obtained using forces from DFT and NEP model using a $6 \times 6 \times 2$ supercell and the PHONOPY package[71].

The reference data obtained through DFT calculations is available in the form of ASE sqlite databases on zenodo at https://doi.org/10.5281/zenodo.13284738. The record also includes the NEP model in a format suitable for the GPUMD package.

MDs and autocorrelation functions
To sample the ACF in Eq. (11), we employed supercells comprising $74 \times 74 \times 23$ primitive unit cells, corresponding to 1,007,582 atoms in the defect configurations. For each temperature, we carried out simulations using 50 different initial configurations that were obtained by NVT simulations at the 0 K lattice parameters as predicted by the NEP model, i.e., $a = 3.080$ Å and $c = 10.082$ Å. For each of these a MD simulation in the NVE ensemble was conducted for 40 ps. The ACF was evaluated up to a time lag of 12 ps. Furthermore, in computing the average of Eq. (11), the time was

reset to zero every 0.5 ps. In total, the average of the ACF was computed over 1500 trajectories, thus corresponding to a total sampling time of 1500×40 ps = 60 ns. The damping was effectively zero for the very large systems due to the natural decay of the ACF. The lower frequency cutoff for evaluation of $F(\omega)$ was 5 meV to avoid amplifying low energy noise by dividing with very small numbers.

For simplicity of implementation, in the NEP model file nep.txt (available on zenodo at https://doi.org/10.5281/zenodo.13284738) we refer to the atomic species that surround the defect by other chemical species as follows: $Si_{gs} \rightarrow P$, $C_{gs} \rightarrow N$, $Si_{ex} \rightarrow S$, and $C_{ex} \rightarrow O$. This allows one to use GPUMD and ASE without modification. To ensure that the dynamics are still sampled correctly, the masses are set explicitly in the input structure files to those of Si and C.

To sample the energy difference between the ground and excited states efficiently, we use the observer functionality of GPUMD, which allows one to evaluate the energy (and related properties) using additional NEP models. To obtain the energy of the ground state when sampling on the excited state, we created a version of the nep.txt file, in which the ground and excited state species were swapped using functionality from CALORINE.

Effect of choice of prefactor

Since the sampling here is done using classical MD simulations the phonon mode occupations follow classical statistics, yielding the classical ACF, Eq. (11). The transition from the classical to the quantum ACF is approximated via Eq. (13), which involves the choice of the prefactor $f(\beta\omega)$. Here, in line with earlier work[42] we chose the harmonic prefactor $f(\beta\omega) = \beta\omega/2$, rather than the so-called standard prefactor $\tanh(\beta\omega/2)$[44].

When using the harmonic prefactor the main peak of the spectral density function at about 30 meV exhibits a weak temperature dependence while at higher energies (≥ 60 meV) the spectral density is almost temperature independent (Figs. 5 and S4c). By contrast, when using the standard prefactor, the temperature dependence is significant for all energies (Fig. S4d). This prefactor saturates at unity for $\beta\omega/2 \gtrsim 2$, and thus has little effect on phonons with energies above 50 meV for the 70 K and 150 K spectral densities.

The good agreement with reference optical emission spectra as well as the consistency between the Stokes shifts computed using static configurations and the spectral distribution function, show, however, the harmonic prefactor ($f(\beta\omega) = \beta\omega/2$) to be the suitable choice for the present system. The latter balances the classical ACF to make it almost fully temperature-independent. This implies that the temperature dependence of the spectral density (Fig. S4c) and emission line shape (Fig. 6a) originate from other parts of the cumulant rather than from the spectral density.

Data availability

The NEP model as well as the database of DFT calculations used to train this model are available on zenodo at https://doi.org/10.5281/zenodo.13284738.

References

1. Maiman, T. H. Stimulated optical radiation in ruby. *Nature* **187**, 493 (1960).
2. Gellermann, W. Color center lasers. *J. Phys. Chem. Solids* **52**, 249 (1991).
3. McKittrick, J. & Shea-Rohwer, L. E. Review: Down conversion materials for solid-state lighting. *J. Am. Ceram. Soc.* **97**, 1327 (2014).
4. Lin, Y.-C., Karlsson, M. & Bettinelli, M. Inorganic phosphor materials for lighting. In: *Photoluminescent Materials and Electroluminescent Devices*, edited by N. Armaroli and H. J. Bolink https://doi.org/10.1007/978-3-319-59304-3_10 (Springer International Publishing, Cham, 2017) pp. 309–355.
5. Nikl, M. & Yoshikawa, A. Recent R&D trends in inorganic single-crystal scintillator materials for radiation detection. *Adv. Opt. Mater.* **3**, 463 (2015).
6. Yanagida, T., Kato, T., Nakauchi, D. & Kawaguchi, N. Fundamental aspects, recent progress and future prospects of inorganic scintillators. *Jpn. J. Appl. Phys.* **62**, 010508 (2022).
7. Weber, J. R. et al. Quantum computing with defects. *Proc. Natl Acad. Sci.* **107**, 8513 (2010).
8. Awschalom, D. D., Hanson, R., Wrachtrup, J. & Zhou, B. B. Quantum technologies with optically interfaced solid-state spins. *Nat. Photonics* **12**, 516 (2018).
9. Wolfowicz, G. et al. Quantum guidelines for solid-state spin defects. *Nat. Rev. Mater.* **6**, 906 (2021).
10. Doherty, M. W. et al. The nitrogen-vacancy colour centre in diamond. *Phys. Rep.* **528**, 1 (2013).
11. Castelletto, S. Silicon carbide single-photon sources: challenges and prospects. *Mater. Quantum Technol.* **1**, 023001 (2021).
12. Grosso, G. et al. Tunable and high-purity room temperature single-photon emission from atomic defects in hexagonal boron nitride. *Nat. Commun.* **8**, 705 (2017).
13. Aharonovich, I., Englund, D. & Toth, M. Solid-state single-photon emitters. *Nat. Photonics* **10**, 631 (2016).
14. Gruber, A. et al. Scanning confocal optical microscopy and magnetic resonance on single defect centers. *Science* **276**, 2012 (1997).
15. Tran, T. T. et al. Robust multicolor single photon emission from point defects in hexagonal boron nitride. *ACS Nano* **10**, 7331 (2016).
16. Wigger, D. et al. Phonon-assisted emission and absorption of individual color centers in hexagonal boron nitride. *2D Mater.* **6**, 035006 (2019).
17. Shang, Z. et al. Local vibrational modes of Si vacancy spin qubits in SiC. *Phys. Rev. B* **101**, 144109 (2020).
18. Udvarhelyi, P. et al. Vibronic states and their effect on the temperature and strain dependence of silicon-vacancy qubits in 4H-SiC. *Phys. Rev. Appl.* **13**, 054017 (2020).
19. Alkauskas, A., Buckley, B. B., Awschalom, D. D. & de Walle, C. G. V. First-principles theory of the luminescence lineshape for the triplet transition in diamond nv centres. *N. J. Phys.* **16**, 073026 (2014).
20. Linderälv, C., Wieczorek, W. & Erhart, P. Vibrational signatures for the identification of single-photon emitters in hexagonal boron nitride. *Phys. Rev. B* **103**, 115421 (2021).
21. Hashemi, A. et al. Photoluminescence line shapes for color centers in silicon carbide from density functional theory calculations. *Phys. Rev. B* **103**, 125203 (2021).
22. Jin, Y. et al. Photoluminescence spectra of point defects in semiconductors: validation of first-principles calculations. *Phys. Rev. Mater.* **5**, 084603 (2021).
23. Markham, J. J. Interaction of normal modes with electron traps. *Rev. Mod. Phys.* **31**, 956 (1959).
24. Miyakawa, T. & Dexter, D. L. Phonon sidebands, multiphonon relaxation of excited states, and phonon-assisted energy transfer between ions in solids. *Phys. Rev. B* **1**, 2961 (1970).
25. Alkauskas, A., Lyons, J. L., Steiauf, D. & Van de Walle, C. G. First-principles calculations of luminescence spectrum line shapes for defects in semiconductors: the example of GaN and ZnO. *Phys. Rev. Lett.* **109**, 267401 (2012).
26. Poncé, S., Jia, Y., Giantomassi, M., Mikami, M. & Gonze, X. Understanding thermal quenching of photoluminescence in oxynitride phosphors from first principles. *J. Phys. Chem. C* **120**, 4040 (2016).
27. Exarhos, A. L., Hopper, D. A., Grote, R. R., Alkauskas, A. & Bassett, L. C. Optical signatures of quantum emitters in suspended hexagonal boron nitride. *ACS Nano* **11**, 3328 (2017).
28. Razinkovas, L., Doherty, M. W., Manson, N. B., Van de Walle, C. G. & Alkauskas, A. Vibrational and vibronic structure of isolated point defects: The nitrogen-vacancy center in diamond. *Phys. Rev. B* **104**, 045303 (2021).
29. Linderälv, C., Åberg, D. & Erhart, P. Luminescence quenching via deep defect states: a recombination pathway via oxygen vacancies in Ce-doped YAG. *Chem. Mater.* **33**, 73 (2021).

30. Bouquiaux, J. et al. Importance of long-range channel Sr displacements for the narrow emission in $SrLi_2Al_2O_2N_2:Eu_{2+}$ phosphor. *Adv. Opt. Mater.* **9**, 2100649 (2021).

31. Jia, Y., Poncé, S., Miglio, A., Mikami, M. & Gonze, X. Beyond the one-dimensional configuration coordinate model of photoluminescence. *Phys. Rev. B* **100**, 155109 (2019).

32. Son, N. T. et al. Divacancy in 4H-SiC. *Phys. Rev. Lett.* **96**, 055501 (2006).

33. Christle, D. J. et al. Isolated electron spins in silicon carbide with millisecond coherence times. *Nat. Mater.* **14**, 160 (2015).

34. Christle, D. J. et al. Isolated spin qubits in SiC with a high-fidelity infrared spin-to-photon interface. *Phys. Rev. X* **7**, 021046 (2017).

35. Radulaski, M. et al. Scalable quantum photonics with single color centers in silicon carbide. *Nano Lett.* **17**, 1782 (2017).

36. Wang, J. et al. Bright room temperature single photon source at telecom range in cubic silicon carbide. *Nat. Commun.* **9**, 4106 (2018).

37. Baiardi, A., Bloino, J. & Barone, V. General time dependent approach to vibronic spectroscopy including Franck-Condon, Herzberg-Teller, and Duschinsky effects. *J. Chem. Theory Comput.* **9**, 4097 (2013).

38. Gastegger, M., Behler, J. & Marquetand, P. Machine learning molecular dynamics for the simulation of infrared spectra. *Chem. Sci.* **8**, 6924 (2017).

39. Xu, N. et al. Tensorial properties via the neuroevolution potential framework: fast simulation of infrared and Raman spectra. *J. Chem. Theory Comput.* **20**, 3273 (2024).

40. Mukamel, S. On the semiclassical calculation of molecular absorption and fluorescence spectra. *J. Chem. Phys.* **77**, 173 (1982).

41. Islampour, R. & Mukamel, S. Line broadening in rigid and nonrigid clusters and molecular electronic spectra. The spectral density formalism. *J. Chem. Phys.* **80**, 5487 (1984).

42. Valleau, S., Eisfeld, A. & Aspuru-Guzik, A. On the alternatives for bath correlators and spectral densities from mixed quantum-classical simulations. *J. Chem. Phys.* **137**, 224103 (2012).

43. Anda, A., De Vico, L., Hansen, T. & Abramavičius, D. Absorption and fluorescence lineshape theory for polynomial potentials. *J. Chem. Theory Comput.* **12**, 5979 (2016).

44. Egorov, S. A., Everitt, K. F. & Skinner, J. L. Quantum dynamics and vibrational relaxation. *J. Phys. Chem. A* **103**, 9494 (1999).

45. Loco, D. & Cupellini, L. Modeling the absorption lineshape of embedded systems from molecular dynamics: a tutorial review. *Int. J. Quantum Chem.* **119**, e25726 (2019).

46. Zuehlsdorff, T. J., Montoya-Castillo, A., Napoli, J. A., Markland, T. E. & Isborn, C. M. Optical spectra in the condensed phase: Capturing anharmonic and vibronic features using dynamic and static approaches. *J. Chem. Phys.* **151**, 074111 (2019).

47. Falk, A. L. et al. Electrically and mechanically tunable electron spins in silicon carbide color centers. *Phys. Rev. Lett.* **112**, 187601 (2014).

48. Csóré, A., Ivanov, I. G., Son, N. T. & Gali, A. Fluorescence spectrum and charge state control of divacancy qubits via illumination at elevated temperatures in 4H silicon carbide. *Phys. Rev. B* **105**, 165108 (2022).

49. Davidsson, J. et al. First principles predictions of magneto-optical data for semiconductor point defect identification: the case of divacancy defects in 4H-SiC. *N. J. Phys.* **20**, 023035 (2018).

50. Westermayr, J. & Marquetand, P. Machine learning for electronically excited states of molecules. *Chem. Rev.* **121**, 9873 (2021).

51. Axelrod, S., Shakhnovich, E. & Gómez-Bombarelli, R. Excited state non-adiabatic dynamics of large photoswitchable molecules using a chemically transferable machine learning potential. *Nat. Commun.* **13**, 3440 (2022).

52. Fransson, E., Wiktor, J. & Erhart, P. Phase transitions in inorganic halide perovskites from machine-learned potentials. *J. Phys. Chem. C.* **127**, 13773 (2023).

53. Pegolo, P. & Grasselli, F. Thermal transport of glasses via machine learning driven simulations. *Front. Mater.* **11**, https://doi.org/10.3389/fmats.2024.1369034 (2024).

54. Erhard, L. C., Rohrer, J., Albe, K. & Deringer, V. L. Modelling atomic and nanoscale structure in the silicon–oxygen system through active machine learning. *Nat. Commun.* **15**, 1927 (2024).

55. Fan, Z. et al. Neuroevolution machine learning potentials: combining high accuracy and low cost in atomistic simulations and application to heat transport. *Phys. Rev. B* **104**, 104309 (2021).

56. Fan, Z. Improving the accuracy of the neuroevolution machine learning potential for multi-component systems. *J. Phys. Condens. Matter* **34**, 125902 (2022).

57. Fan, Z. et al. GPUMD: a package for constructing accurate machine-learned potentials and performing highly efficient atomistic simulations. *J. Chem. Phys.* **157**, 114801 (2022).

58. Skone, J. H., Govoni, M. & Galli, G. Self-consistent hybrid functional for condensed systems. *Phys. Rev. B* **89**, 195112 (2014).

59. Blasse, G. & Grabmaier, B. C. Luminescent materials https://doi.org/10.1007/978-3-642-79017-1 (Springer-Verlag, 1994).

60. Born, M. & Huang, K. Dynamical theory of crystal lattices (Oxford University Press, 1954).

61. Hele, T. J. H., Willatt, M. J., Muolo, A. & Althorpe, S. C. Communication: Relation of centroid molecular dynamics and ring-polymer molecular dynamics to exact quantum dynamics. *J. Chem. Phys.* **142**, 191101 (2015).

62. Blöchl, P. E. Projector augmented-wave method. *Phys. Rev. B* **50**, 17953 (1994).

63. Kresse, G. & Joubert, D. From ultrasoft pseudopotentials to the projector augmented-wave method. *Phys. Rev. B* **59**, 1758 (1999).

64. Kresse, G. & Hafner, J. Ab initio molecular dynamics for liquid metals. *Phys. Rev. B* **47**, 558 (1993).

65. Kresse, G. & Furthmüller, J. Efficient iterative schemes for ab initio total-energy calculations using a plane-wave basis set. *Phys. Rev. B* **54**, 11169 (1996).

66. Kresse, G. & Furthmüller, J. Efficiency of ab-initio total energy calculations for metals and semiconductors using a plane-wave basis set. *Comput. Mater. Sci.* **6**, 15 (1996).

67. Perdew, J. P. et al. Restoring the density-gradient expansion for exchange in solids and surfaces. *Phys. Rev. Lett.* **100**, 136406 (2008).

68. Lindgren, E. et al. calorine: a python package for constructing and sampling neuroevolution potential models. *J. Open Source Softw.* **9**, 6264 (2024).

69. Larsen, A. H. et al. The atomic simulation environment—a python library for working with atoms. *J. Phys.: Condens. Matter* **29**, 273002 (2017).

70. Eriksson, F., Fransson, E. & Erhart, P. The Hiphive package for the extraction of high-order force constants by machine learning. *Adv. Theory Simul.* **2**, 1800184 (2019).

71. Togo, A. First-principles phonon calculations with phonopy and phono3py. *J. Phys. Soc. Jpn.* **92**, 012001 (2023).

Acknowledgements

Author contributions

Funding

Competing interests

The authors declare no competing interests.

Additional information

Supplementary information The online version contains supplementary material available at https://doi.org/10.1038/s41524-025-01565-x.

Correspondence and requests for materials should be addressed to Paul Erhart.

Reprints and permissions information is available at http://www.nature.com/reprints

Publisher's note Springer Nature remains neutral with regard to jurisdictional claims in published maps and institutional affiliations.

Optical line shapes of color centers
in solids from classical autocorrelation functions

Christopher Linderälv,[1,2] Nicklas Österbacka,[1] Julia Wiktor,[1] and Paul Erhart[1,*]

[1] Department of Physics, Chalmers University of Technology, SE-41296, Gothenburg, Sweden

[2] University of Oslo, Department of Physics, Centre for Material Science and Nanotechnology,
P.O. Box 1048, Blindern, Oslo N-0316, Norway

* erhart@chalmers.se

Contents

Supplementary Figures

Fig. S1: Orbitals of the $(\mathbf{V_{Si}V_C})^0_{kk}$ defect in the ground state. (a) Defect level structure and (b–j) corresponding orbitals superimposed on the defect configuration. The orbitals are indexed from lowest to highest energy starting at $n = 1$ for each spin channel. Occupied orbitals are highlighted in blue in (b–j).
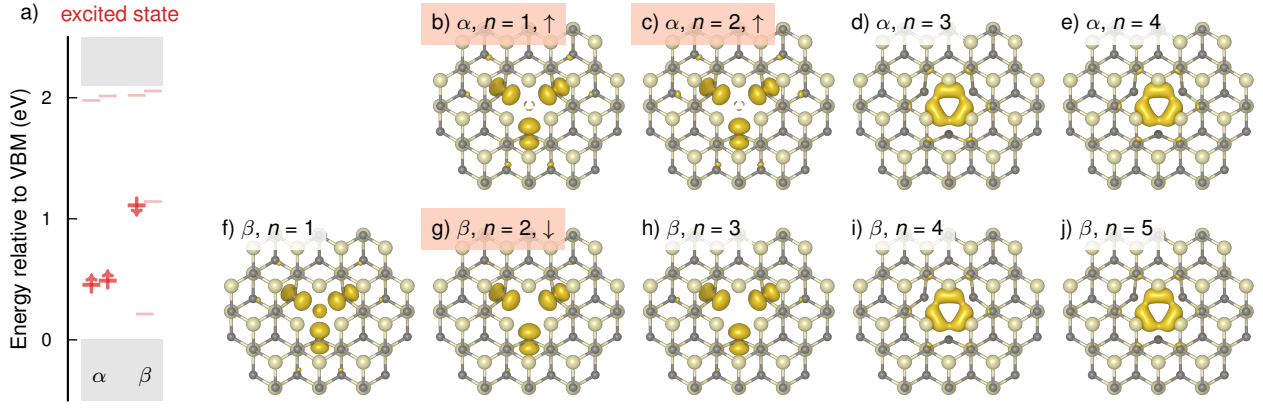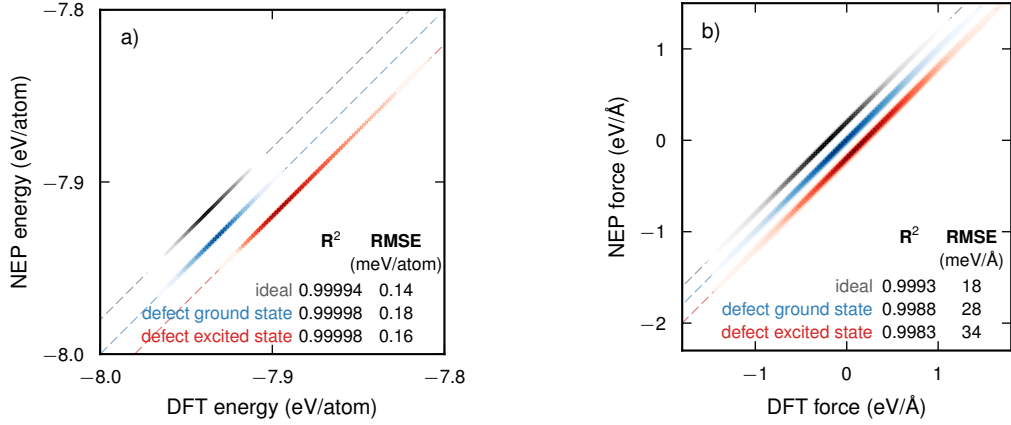
Fig. S2: Orbitals of the $(V_{Si}V_C)^0_{kk}$ defect in the excited state. (a) Defect level structure and (b–j) corresponding orbitals superimposed on the defect configuration. The orbitals are indexed from lowest to highest energy starting at $n = 1$ for each spin channel. Occupied orbitals are highlighted in red in (b–j).

Fig. S3: Parity plots for the machine-learned potential. The data for (a) energy and (b) forces are presented in the form of kernel density estimates comparing results from the neuroevolution potential (NEP) model with density functional theory (DFT) reference data. Coefficients of determination (R^2) and root mean square error (RMSE) for subsets of the data are shown in the tables.
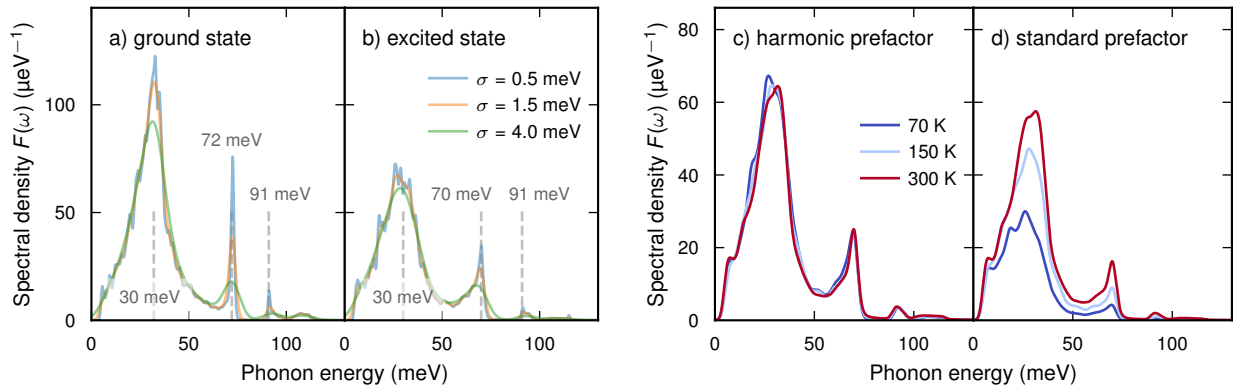

Fig. S4: Effect of broadening and prefactor on the spectral density. (a, b) Spectral densities at 70 K using different levels of broadening. (c, d) Effect of the prefactor $f(\beta\omega)$, see Eq. (13) in the main paper, included for treating quantum effects on the spectral density.
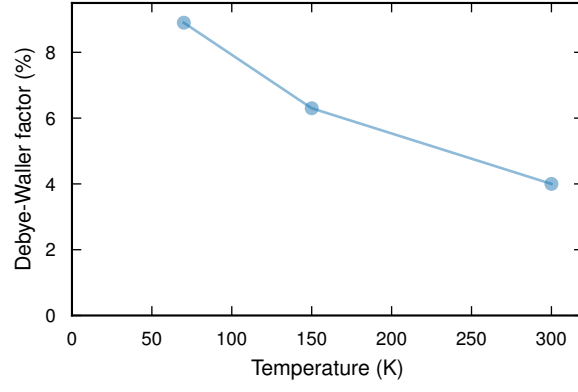
Fig. S5: **Debye-Waller factor.** Debye-Waller factor for the $(V_{Si}V_C)^0_{kk}$ defect as a function of temperature. It was obtained as the integral over the zero-phonon line relative to the full spectrum, which is approach also commonly adopted when analyzing experimental spectra.